published by Ural Federal University
eISSN 2411-1414
chimicatechnoacta.ru

ARTICLE
2024, vol. 11(2), No. 202411208
DOI: 10.15826/chimtech.2024.11.2.08

Photoelectrochemical properties of Pt- and Ir-modified graphitic carbon nitride

Dina V. Markovskaya *, Victoria A. Lomakina, Ekaterina A. Kozlova

Department of heterogeneous catalysis, Boreskov Institute of Catalysis, Novosibirsk 630090, Russia
* Corresponding author: madiva@catalysis.ru

This paper belongs to a Regular Issue.

Abstract

In this work, the photoelectrochemical properties of g-C_3N_4 modified with Pt, Ir and Ir/Pt bimetallic co-catalysts were studied. All prepared photoelectrodes were tested in a two-electrode cell by cyclic voltammetry, impedance spectroscopy, and the Mott-Schottky method. First, the optimal electrolyte (triethanolamine, NaCl, NaOH, Na_2SO_4) was selected. The highest photocurrents were recorded in 0.5 M Na_2SO_4. This electrolyte was used for the subsequent tests. Second, the photoelectrodes loaded with the noble metals are studied. It was shown that in case of monometallic co-catalysts, the deposition of noble metal is accompanied by the decrease of the short-circuit current density and the growth of open-circuit voltage. The simultaneous presence of bimetallic co-catalysts can significantly affect the semiconductor electron structure and photogalvanic properties. Some correlations between the short-circuit current density and the oxidation state of the noble metals were found. A linear correlation between Pt^0/Pt^0+Pt^{2+} and J_{sc} was observed. It was also shown that the presence of iridium in Ir^{3+} form favors the photocurrent generation. The highest values of the photocurrent were obtained for g-C_3N_4 and were equal to 0.57 mA/cm^2.

Keywords

g-C_3N_4
noble metals
photoelectrochemistry
visible light
cyclic voltammetry
impedance spectroscopy

Received: 08.04.24
Revised: 27.04.24
Accepted: 27.04.24
Available online: 07.05.24

Key findings

- 0.5 M Na_2SO_4 is an ideal electrolyte for testing g-C_3N_4-based photoelectrodes.
- Pt- and Ir- modified samples are more active than ones modified with Ir and Pt simultaneously.
- Noble metal deposition leads to the increase in open circuit voltage.

1. Introduction

The ever-increasing demand for energy, combined with modern environmental requirements and dwindling reserves of natural resources, necessitates the search for alternative renewable energy sources. From this point of view, the usage of solar energy is a promising way of e solving the energy problem. To collect, to store, and to convert solar energy into other forms, photoelectrochemical technologies seem to be among the most attractive and promising: already existing solar panels and photoelectrochemical cells can convert solar energy into the electrical one. However, creating such devices is a non-trivial task that requires a competent approach to the choice of the materials used [1].

The basis of any photoelectrochemical system is a semiconductor that absorbs photons, resulting in the formation of electron – hole pairs. The addition of an external potential leads to the photocurrent generation. Among all the semiconductors, carbon-containing materials are interesting because of their band structure and chemical stability [2]. Among the carbon-containing materials, special attention should be paid to graphitic carbon nitride. This semiconductor has suitable valence and conduction bands positions, high electronic conductivity, thermal and chemical stability. In addition, its optical properties allow only visible light to be used to activate the semiconductor. However, the efficiency and stable operation time of photoelectrochemical cells based on carbon nitride are quite low due to the high recombination rate of holes and elec-

trons and low mobility and charge concentration at the material/electrolyte interface. Obviously, these aspects severely limit the use of g-C_3N_4 for photo- and photoelectrocatalysis [1, 3, 4].

It should be noted that the same strategies are used to improve both the photocurrents and the photocatalytic activity. The deposition of noble metals on the photoelectrode surface leads to an improvement in the short-circuit current density [5, 6]. In [4] it was shown that Pt deposition on g-C_3N_4 doubled the photocurrent value due to the enhancement of the electronic conductivity. This dependence was demonstrated in [7, 8], where the photocatalytic hydrogen production was improved after Pt deposition. This was due to the decrease in the contact resistance at the semiconductor/electrolyte interface and the effective spatial separation of charges. Researchers in [9] came to similar conclusions when studying the dependence of the photocurrent density on the externally applied potential. The same effects may be caused by other noble metals. For example, the deposition of Ag and Au increased the photocurrent compared to the unmodified carbon nitride [10, 11]. Unfortunately, there is insufficient information about several noble metals such as Ir. It is also interesting to study bimetallic co-catalysts such as Pt and Ir.

It is well known that the composition of the electrolyte is the main determinant of all photoelectrochemical properties due to the different mechanisms of charge transport and the values of the forces causing data transport [12]. Graphitic carbon nitride is often tested in sodium sulphate solutions (0.1–0.5 M) [13–33]. Researchers are more likely to use sodium hydroxide [34] or sodium chloride [35] solutions. However, there are no any comprehensive works describing the choice of electrolyte in which most of the analytical signal values are obtained. It should be noted that high currents are often recorded in the solutions used to test other key properties such as the photocatalytic one [35]. For this purpose, aqueous solutions of thiethanolamine (TEOA) are often used for testing the photocatalytic activity. From this point of view, it is interesting to compare the photoelectrochemical properties in inorganic solutions and in TEOA. Therefore, the aim of our work is to optimise the electrolyte solution and to study the photoelectrochemical properties of graphitic carbon nitride modified with Pt, Ir, and Pt/Ir simultaneously.

2. Experimental

2.1. Photocatalyst preparation

Graphitic carbon nitride is prepared as follows [36]. 40.5 g of melamine and 41.5 g of cyanuric acid are suspended in 0.3 L of water and heated at 90 °C 12 h with continuous stirring. The compound obtained is washed and dried under vacuum and then calcined at 550 °C for 1 h at a heating rate of 1 °C/min.

The platinum-containing photocatalysts are prepared as follows [36]. 2.5 g of as-prepared g-C_3N_4 is suspended in 40 ml of acetone; after that acetone solution of $(Me_4N)_2[Pt_2(\mu\text{-}OH)_2(NO_3)_8]$ is added. The resulting suspension is stirred for 12 h at room temperature. The precipitate is then collected, washed with acetone and dried in air. This precursor is calcined in a hydrogen atmosphere at 400 °C for 1 h. The photocatalysts obtained are denoted as 0.1 Pt-PC (0.1% Pt/g-C_3N_4) or 0.5 Pt-PC (0.5% Pt/g-C_3N_4).

The Ir-modified samples are synthesised by the following method [36]. 500 mg of g-C_3N_4 is suspended in acetone; then the solution of *fac*-$[Ir(H_2O)_3(NO_2)_3]$ in acetone is added. This suspension is mixed, undergoes the ultrasound treatment and is dried at 200°C to remove acetone. After that, the precursor is calcined at 350 °C for 60 min. The prepared photocatalysts are labelled as 0.5 Ir-PC (0.5% Ir/g-C_3N_4).

The photocatalysts containing both Pt and Ir are prepared by the same method. The photocatalysts 0.1 Pt-PC or 0.5 Pt-PC are used instead of g-C_3N_4, and the samples obtained are denoted as *y*Ir–0.1 Pt-PC or *y*Ir–0.5 Pt-PC, respectively, where *y* is a weight content of Ir.

The physicochemical properties of the prepared photocatalysts were described earlier [36].

2.2. Testing of photoelectrochemical properties

The photoelectrochemical properties are studied in a two-electrode photoelectrochemical cell using a P-45Kh potentiostat–galvanostat (Russia) equipped with an FRA-24M electrochemical impedance measurement module. The working electrodes are prepared by the following way. 30 mg of the examined photocatalysts is deposited by a drop-casting method described earlier [37]. The synthesised photoelectrodes are labeled in the same way as the corresponding photocatalysts without 'PC'. For example, the 0.1 Pt electrode is prepared from 0.1 Pt-PC. The counter electrode is Cu_2S/brass [17]. Different solutions such as 0.1 M Na_2SO_4, 0.5 M Na_2SO_4, 0.1 M NaOH, 0.1 M NaCl, 10 vol.% TEOA, and 10 vol.% TEOA + 0.1 M NaOH are used as electrolytes. To improve contacts, the electrodes are compressed. The photoelectrochemical cell is illuminated with a 425-LED (20 mW/cm^2). All electrodes are analysed by cyclic voltammetry (scan rate of 0.02 V/s, potential range from –0.8 to 0.8 V), impedance spectroscopy (frequency range of 0.8–10^5 Hz; amplitude of 10 mV; external potential of 200 mV), and the Mott–Schottky method (potential range from –0.6 to 0.7 V; amplitude of 10 mV; frequency of 1000 Hz).

3. Results and discussion

3.1. Optimisation of the electrolyte to study the photoelectrochemical properties of graphitic carbon nitride

The photoelectrochemical properties of g-C_3N_4 were studied in Na_2SO_4 (0.1 M and 0.5 M), 0.1 M NaOH, 0.1 M NaCl, 10 vol.% TEOA, and 10 vol.% TEOA + 0.1 M NaOH. Figure 1 depicts the corresponding cyclic voltammograms.

 DOI: 10.15826/chimtech.2024.11.2.08

Figure 1 shows that all studied photoelectrodes investigated are stable under the testing conditions. Additionally, there are no peaks that are typical of oxidation – reduction processes. From the second curve, the photovoltaic parameters were calculated and listed in Table 1.

Table 1 and Figure 1 show that the photocurrent measured in TEOA solution is lower than that measured in inorganic solutions. This may be due to the low dielectric constant and degree of ionisation [1]. It is well known that organic compounds have non-electrolyte properties; therefore, electron transport is difficult in organic media. The addition of sodium hydroxide increases the photocurrent density from 0.008 mA/cm² to 0.036 mA/cm². This growth is supported by the addition of different ions in which electron transport is more effective. Moreover, the photocurrents recorded in pure NaOH without any impurities are higher than those measured in the mixture of triethanolamine and sodium hydroxide. The prepared photoelectrodes were also tested in sodium chloride and sodium sulphate. It should be noted that the short-circuit current densities obtained in 0.1 M solutions of inorganic compounds increase with increasing anion mobility. The high photocurrents were observed for 0.1 M NaOH. Unfortunately, sodium hydroxide can alter the structure of graphitic carbon nitride, so it is undesirable to use it for testing this material. Higher photocurrents were obtained in Na_2SO_4 solution compared to NaCl, so we chose sodium sulphate as the electrolyte for testing the photoelectrochemical properties of g-C_3N_4. Researchers often use 0.1 M and 0.5 M solutions, so we tested these solutions. It should be noted that the growth of salt concentration leads to the change in slope of the corresponding cyclic voltammograms due to the different resistances and electroconductivity in the tested solutions. High slope of the voltammogram obtained in 0.5 M Na_2SO_4 compared to 0.1 M Na_2SO_4 indicates low resistivity and good photocurrents. By the way, the best results were obtained in 0.5 M Na_2SO_4, where the highest value of the short-circuit current density is 0.571 mA/cm² as seen in Table 1. These solutions were used in the following experiments.

Another photovoltaic parameter is the open circuit voltage. This value can be defined as the voltage in the absence of any current and reflects the energetic aspect of the conversion of light energy into electricity. It is well known that, at low resistivity, the open-circuit voltage is directly proportional to the logarithm of the short-circuit current density [39]. Figure 2 confirms this for the systems tested. The fill factor reflects the effect of ohmic losses in the photoelectrochemical cell. Table 1 shows that the fill factor varies from 23% to 28% and is slightly dependent on the electrolyte type. The power conversion efficiency (PCE) defines the efficiency of converting light energy into electricity. Table 1 shows that the main trends in PCE changes are the same as for J_{sc} and are caused by the same reasons. The highest PCE of 0.86% was determined for the photoelectrochemical cell with 0.5 M Na_2SO_4.

3.2. The influence of Ir and Pt co-catalysts on the photoelectrochemical properties of the graphitic carbon nitride

The noble metals such as Ir or Pt were deposited on the g-C_3N_4 surface. The cyclic voltammograms of all the samples tested in 0.5 M Na_2SO_4 are shown in Figure 3. It can be seen that the loading of noble metals leads to a decrease of the photocurrents compared to pristine g-C_3N_4. The presence of two noble metals on the photoelectrode surface also reduces the photocurrent values. It should be noted that the deposition of noble metals does not affect the stability of C_3N_4: no peaks are observed on the CVA curves for the photoelectrodes tested. However, there are some interesting features in the cyclic voltammograms. Figure 3a shows that the linear correlation between potential and current density is found for all curves.

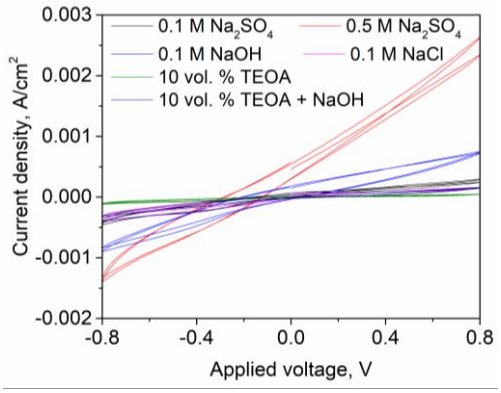

Figure 1 The cyclic voltammograms of graphitic carbon nitride tested in different electrolytes.

Table 1 The photoelectrochemical properties of g-C_3N_4 recorded in the photoelectrochemical cell with different electrolytes.

Electrolyte	J_{sc} (mA/cm²)	V_{oc} (mV)	FF (%)	PCE (%)
10 vol.% TEOA	0.008±0.001	100±10	27±5	<0.01
10 vol.% TEOA + 0.1 M NaOH	0.036±0.003	115±12	24±5	0.020±0.003
0.1 M NaCl	0.028±0.003	120±12	28±6	0.020±0.003
0.1 M Na_2SO_4	0.060±0.006	167±17	25±5	0.051±0.009
0.1 M NaOH	0.189±0.02	205±21	26±5	0.20±0.03
0.5 M Na_2SO_4	0.57±0.06	289±29	23±4	0.9±0.1

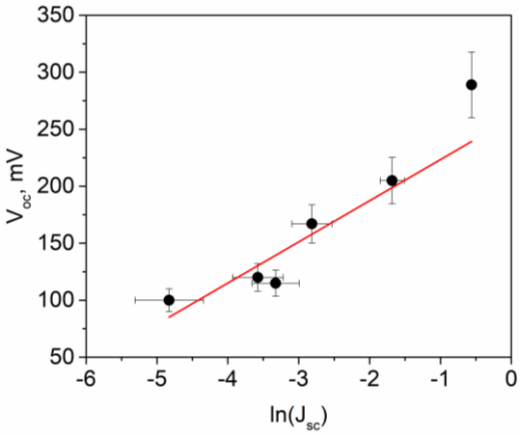

Figure 2 The correlation between the open-circuit voltage and logarithm of the short-circuit current density.

 DOI: 10.15826/chimtech.2024.11.2.08

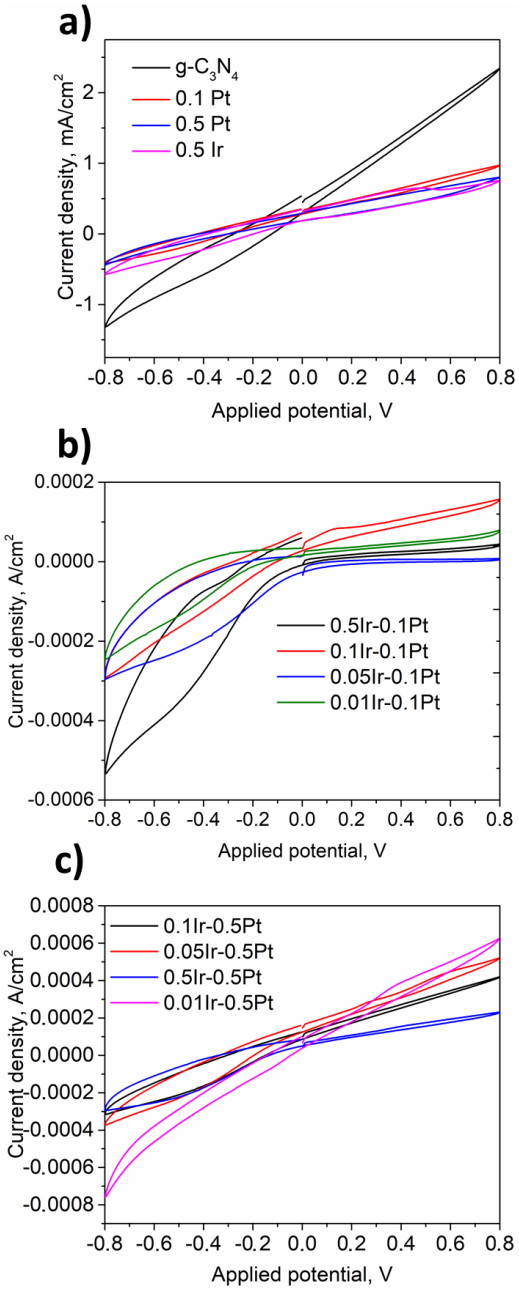

Figure 3 Cyclic voltammograms obtained in the photoelectrochemical cell with g-C_3N_4, 0.1% Pt/g-C_3N_4, and 0.5Ir%/g-C_3N_4 (a); 0.5Ir–0.1Pt, 0.1Ir–0.1Pt, 0.05Ir–0.1Pt, 0.01Ir–0.1Pt (b); 0.5Ir–0.5Pt, 0.1Ir–0.5Pt, 0.05Ir–0.5Pt, 0.01Ir–0.5Pt (c) as the working electrode. Correlation between the open-circuit voltage and logarithm of the short-circuit current density.

Figures 3b and 3c show curves in which two regions can be distinguished. The first region is a linear (or near linear) curve described by Ohm's law. It lies from 0 V to 0.8 V for 0.5Ir–0.1Pt, 0.1Ir–0.1Pt, 0.05Ir–0.1Pt, 0.01Ir–0.1Pt and from –0.6 to 0.8V for 0.5Ir–0.5Pt, 0.1Ir–0.5Pt, 0.05Ir–0.5Pt, 0.01Ir–0.5Pt. The second region is at high negative applied potentials for the samples tested. In this region the I–V dependence is quadratic and can be attributed to the additional process of electron transport between g-C_3N_4 and two noble metals.

The photovoltaic parameters are calculated from the CVA data, and the results are listed in Table 2. Table 2 shows that the deposition of noble metal is accompanied by a decrease in the short-circuit current density. This unusual fact can be explained as follows. The short-circuit current density measures the current flowing in the external circuit from the FTO to the counter electrode at zero potential. It is known that the conduction band (CB) position of FTO is –0.54 eV [40], g-C_3N_4 is –1.25 eV [41], while the valence band (VB) of FTO is 3.2 eV, g-C_3N_4 – 1.45 eV. Thus, when the working electrode is irradiated with a diode (λ = 425 nm), photogenerated electrons and holes are formed. Since the CB position of the FTO is lower than that of the g-C_3N_4, the photogenerated electrons migrate to the FTO and into the external circuit, as shown in Figure 4. When the noble metal is deposited, the photogenerated electrons can migrate to the metallic co-catalyst. The electron transfer from Pt to the FTO is less thermodynamically favoured than that from g-C_3N_4. In this way, the deposition of noble metal reduces the short-circuit current density. Furthermore, this effect increases with increasing noble metal content: J_{sc} of 0.1 Pt and 0.5 Pt are 0.353 and 0.280 mA/cm² respectively. It should be noted that the decrease in short-circuit current density is less pronounced for Ir-modified electrons. Table 2 shows that the J_{sc} values of 0.5 Pt and 0.5 Ir are 0.280 and 0.339 mA/cm² respectively. This may be due to the differences in the work function of the noble metals: for Ir this value is 0.4 eV lower than for Pt [42]; therefore, electron transfer to Ir is less thermodynamically favoured than that to Pt.

Let us consider the changes in other photogalvanic parameters after noble metal deposition. Table 2 shows that the loading of Pt or Ir leads to an increase in the open circuit potential. For Pt modified samples 0.1 Pt and 0.5 Pt, Voc is higher than 400 mV and is weakly dependent on the Pt weight content. For 0.5 Ir the open circuit potential is lower than for 0.5 Pt. This result can be associated with the amount of energy required for electron transfer from the corresponding particle. The work function of metallic co-catalysts and g-C_3N_4 [43] decreases in the following sequence: Pt > Ir > g-C_3N_4. Thus, the energy required for electron transfer from the electrode to the electrolyte and the open circuit voltage (energy reserve during the photoelectrochemical process) decrease in the same sequence.

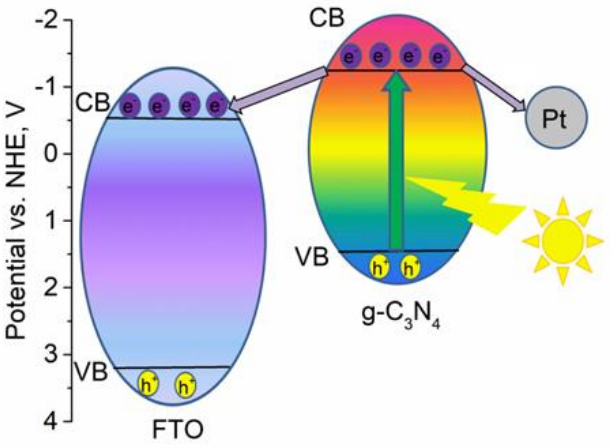

Figure 4 Scheme of electron transfer realised under the illumination of photoelectrodes 0.1 Pt or 0.5 Pt.

 DOI: 10.15826/chimtech.2024.11.2.08

Table 2 The photogalvanic properties of g-C_3N_4 with deposited Pt and/or Ir co-catalysts, and the chemical state of the deposited metals estimated by the XPS method.

Working electrode	[Pt°]/ ([Pt°] + [Pt²⁺]) (%)	[Ir°]/ ([Ir°] + [Ir³⁺]) (%)	J_{sc} (mA/cm²)	V_{oc} (mV)	FF (%)	PCE (%)
g-C_3N_4	-[a]	–	0.57±0.06	289±29	23±4	0.9±0.1
0.1 Pt		–	0.35±0.04	434±44	25±5	0.80±0.14
0.5 Pt		–	0.28±0.03	411±41	26±5	0.60±0.10
0.5 Ir	–	10	0.34±0.03	386±39	25±5	0.68±0.12
0.01Ir–0.1Pt	60	–	0.028±0.003	448±45	48±10	0.07±0.01
0.05Ir–0.1Pt	53	33	0.016±0.002	312±31	43±9	0.028±0.005
0.1Ir–0.1Pt	39	13	0.077±0.008	284±28	25±5	0.11±0.02
0.5Ir–0.1Pt	24	14	0.077±0.008	238±24	30±6	0.10±0.02
0.01Ir–0.5Pt	60	–	0.11±0.01	390±39	33±7	0.11±0.02
0.05Ir–0.5Pt	68	0	0.13±0.01	339±34	28±6	0.23±0.04
0.1Ir–0.5Pt	57	0	0.12±0.01	333±34	27±6	0.20±0.03
0.5Ir–0.5Pt	50	17	0.085±0.009	281±28	30±6	0.17±0.03

[a] is not identified by the XPS technique.

Table 2 shows that the fill factor of the monometallic photoelectrodes does not change. The trends in the change of the PCE are the same as for the short-circuit current density.

The simultaneous presence of bimetallic co-catalysts can have a significant effect on the semiconductor electronic structure and photogalvanic properties. The values of the photogalvanic parameters obtained are given in Table 2. It should be noted that Ir deposition also leads to a decrease in the short circuit current density. However, the main trends in J_{sc} changes are different between *y*Ir–0.1Pt and *y*Ir–0.5Pt samples. Table 2 and Figure 5 show that in the case of *y*Ir–0.1Pt, the increase in Ir content from 0.01% to 0.05% leads to an increase in the short-circuit current density, after which the J_{sc} value increases with increasing Ir content and reaches a plateau. The opposite trend is observed for the *y*Ir–0.5Pt samples: this dependence passes through a maximum at y = 0.05.

It is reasonable to assume that oxidation state and photocurrent are related. The XPS analysis shows that Pt is present in Pt° and Pt^{2+} states, while Ir is present in Iro and Ir^{3+} forms. Table 2 shows the proportions of the metallic forms in the tested photoelectrodes. It is interesting to note that for *y*Ir–0.5Pt the linear correlation between Pt°/Pt°+Pt^{2+} and J_{sc} is observed, as shown in Table 2 and Figure 6. For the first three samples of this set, Ir is only present in ionic form; therefore, its state does not affect the photocurrent density. In the case of *y*Ir–0.1Pt, the relative content of Pt° decreases with y values, while the short-circuit current density changes in a non-monotonic way. This may be due to changes in the Ir state: the Ir^{3+} content and the total Ir content increase with y. Ir_2O_3 is known to be a semiconductor [44]; therefore, it may be involved in various electron transfer processes that improve the photogalvanic properties. This statement can be confirmed by 0.05Ir–0.1Pt and 0.1Ir–0.1Pt. In this case, the relative Pt° content decreases from 53% to 39%, while the short circuit current density and the Ir^{3+} content increase. Overall, the set *y*Ir–0.5Pt is more active compared to *y*Ir–0.1Pt; however, the photoelectrodes with bimetallic co-catalysts are less active than the monometallic ones.

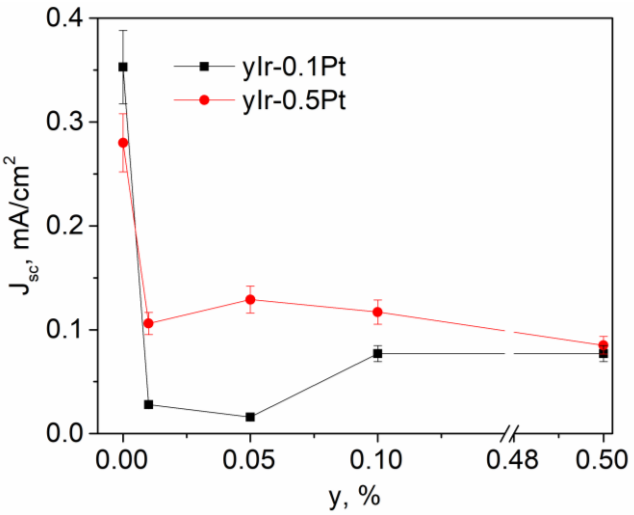

Figure 5 Scheme of electron transfer realised under the illumination of photoelectrodes 0.1 Pt or 0.5 Pt.

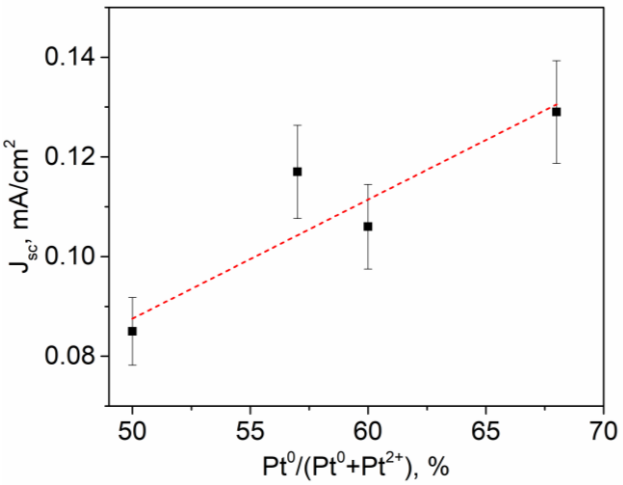

Figure 6 The relationship between the short-circuit current density and Pt° relative content found for the *y*Ir–0.5Pt samples.

 DOI: 10.15826/chimtech.2024.11.2.08

Table 2 also gives information on the open circuit voltage, fill factor and PCE recorded in the photoelectrochemical cell with the working electrodes containing bimetallic co-catalysts. For both sets of samples, the open circuit potential decreases with increasing Ir content in the samples. The energy reserved during the photoelectrochemical process (V_{oc}) increases with the value of the energy required for electron transfer to the external circuit. The work function of Ir is lower than that of Pt, so its deposition reduces the electron work function. For all samples except for 0.01Ir–0.1Pt and 0.05Ir–0.1Pt, the filling factor is from 25% to 30%. The trends in the PCE change are the same as those in the short-circuit current density.

3.3. Stydying Ir and Pt-contained photoelectrodes by the impedance spectroscopy

Impedance spectroscopy can provide some information about the electron transfer in the tested electrodes. All samples were examined by this method. Figure 7 shows the results obtained in Nyquist coordinates. For all samples, the trends in the changes in resistivity and short-circuit current density are opposite to those according to Ohm's law.

It should be noted that the obtained hodographs can be approximated by two semicircles, which could be represented by the equivalent circuit shown in Figure 8 [44]. This circuit is made up of the resistor R_3, which includes the resistance of the FTO and the electrolyte, and the resistors R_1 and R_2, which are responsible for the processes that take place during charge transfer across the interference boundaries. Capacitors C_1 and C_2 in Figure 8 show the double electrical layers that occur at the corresponding interference boundaries. All hodographs are approximated with the equivalent circuit; the data obtained are shown by dotted lines in Figure 7, and the approximation parameters are listed in Table 3.

It is important to identify the nature of the R_1 and R_2 parameters. After the deposition of the noble metal on the surface of C_3N_4 and the formation of the photoelectrode, some new interphase boundaries such as metal/g-C_3N_4, metal/FTO are formed. The changes in R_1 and J_{sc} are antibatic and can be attributed to the metal/FTO boundaries. The higher the metal content and the larger the work function, the more energy is required to transfer electrons from the metal particle to the conducting substrate FTO. The same trend is found for R_2 except for sample 0.5 Ir. This resistance can be supported by the metal/g-C_3N_4 interphase boundary. The sharp increase in resistance R_2 for a sample containing iridium may be due to the presence of two phases – metallic iridium and iridium oxide (see Table 2), whereas 0.1 Pt and 0.5 Pt contain only metallic platinum. The presence of two noble metals on the surface of g-C_3N_4 leads to the formation of new interphase boundaries; therefore, the interpretation of parameters R_1–R_2 may change. Let us consider the main trends in their variation. Tables 2 and 3 show that R1 and the ratio of metallic platinum change symbatically for both *y*Ir–0.1Pt and *y*Ir–0.5Pt sets. As the metallic Pt content increases, the amount of electrons on Pt^0 also increases, so the energy required for electron transfer from Pt nanoparticles increases.

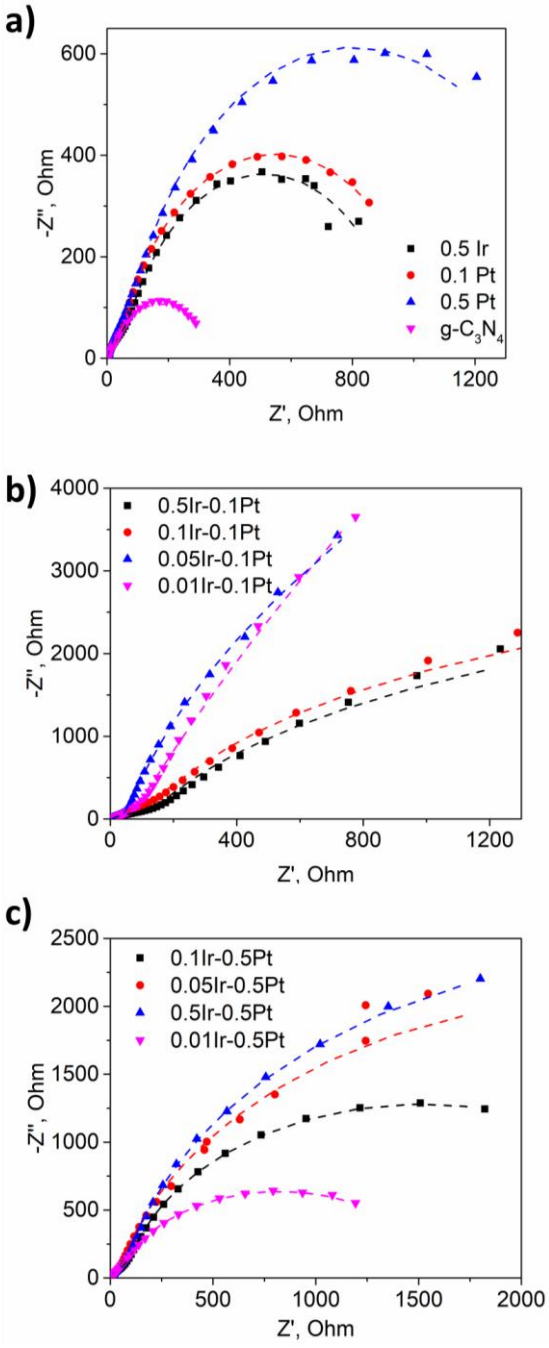

Figure 7 The Nyquist plots measured in the photoelectrochemical cells with g-C_3N_4 and monometallic photoelectrodes (a); *y*Ir–0.1Pt (b); *y*Ir–0.5Pt as working electrodes (c). The external potential is 200 mV, the amplitude is 10 mV. The dots indicate the experimental data; dot lines show their approximation by the equivalent electrical circuit.

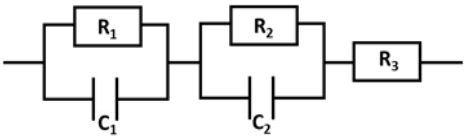

Figure 8 An electrical equivalent circuit used for impedance fitting of the experimental data.

 DOI: 10.15826/chimtech.2024.11.2.08

Table 3 The parameters of the equivalent circuit elements obtained by the approximation of the experimental data.

Working electrode	R_1 (Ohm)	R_2 (Ohm)	R_3 (Ohm)
g-C_3N_4	462±11	15±2	2.41±0.03
0.1 Pt	1017±9	40±2	2.34±0.02
0.5 Pt	1484±29	65±6	3.08±0.03
0.5 Ir	912±8	556±2	2.88±0.02
0.01Ir–0.1Pt	(1.0±0.2)·10^6	64±2	2.32±0.03
0.05Ir–0.1Pt	(3.2±0.1)·10^4	435±1	2.76±0.01
0.1Ir–0.1Pt	(6.1±0.4)·10^3	170±15	3.09±0.05
0.5Ir–0.1Pt	(6.4±0.6)·10^3	121±7	6.84±0.01
0.01Ir–0.5Pt	441±13	(1.3±0.4)·10^3	3.14±0.02
0.05Ir–0.5Pt	(5.0±0.3)·10^3	317±3	3.22±0.05
0.1Ir–0.5Pt	(2.89±0.04)·10^3	83±2	2.44±0.01
0.5Ir–0.5Pt	70±4	(5.6±0.2)·10^3	2.22±0.02

In addition, R_1 reflects the resistance to charge transfer from Pt to the FTO. In the case of *y*Ir–0.1Pt and *y*Ir–0.5Pt except 0.5Ir–0.5Pt, the increase in the amount of Ir_2O_3 leads to a decrease in R_2. Iridium oxide is a semiconductor; therefore, the heterojunctions between g-C_3N_4 and Ir_2O_3, FTO and Ir_2O_3 can be realised. The FTO has the lowest position of the conduction band, so the electron transfer from Ir_2O_3 to the FTO is more easily realised than from Ir. Thus, R_2 can be attributed to the electron transfer from Ir-containing phases to the FTO. As in the previous case, R_3 values are weakly dependent on the photoelectrode composition and include the resistivity.

The impedance data can be presented in Bode plots (see Figure 9). Figure 9 shows that the experimental curves for all samples tested consist of two individual curves. All experimental curves were deconvoluted and the electron lifetime was calculated from the maximum of each peak. The values obtained are given in Table 4. Table 4 shows that for monometallic co-catalysts the J_{sc} values and the electron lifetime τ_1 change simultaneously. For bimetallic co-catalysts, the electron lifetime τ_1 increases with increasing Ir content for both sets. For all samples τ_2 does not change.

In addition, the Mott-Schottky method is used to characterise the samples obtained. Figure 10 shows the typical Mott-Schottky plot. It can be seen that the curve obtained has the linear part with the positive slope. This fact indicates that the sample under investigation is an n-type semiconductor. The positive slope is observed for all the samples tested. Therefore, the deposition of one or two noble metals does not affect the conductivity type. From the linear part of the Mott-Schottky dependence, the flat-band potential and $N{\cdot}\varepsilon$ can be calculated using the following formulae [27]:

$$\frac{1}{C^2} = \frac{2}{\varepsilon \cdot \varepsilon_0 \cdot N \cdot S^2}\left[(V - V_{jb}) - \frac{kT}{e}\right], \quad (1)$$

where ε_0 is the permittivity of vacuum (8.85·10^{-12} F/m), ε is the dielectric constant of the materials, e is the electronic charge (1.60·10^{-19} C), N is the concentration (m^{-3}) of electrons, S is the surface of the irradiated photoelectrodes (m^2), T is the room temperature (K), k is Boltzmann's constant (J/K), V is the electrode potential (V), V_{fb} is the flat-band potential (V), and C is the space charge capacitance (F/m^2).

Table 5 shows that the deposition of 0.1% Pt does not change the flat band potential. The further increase of the Pt amounts up to 0.5 wt.% leads to a decreasing V_{fb}. The same trend is observed for the 0.5 Ir sample. It should be noted that for the electrodes with bimetallic co-catalysts the flat-band potential value is the same as for the corresponding Pt-modified samples.

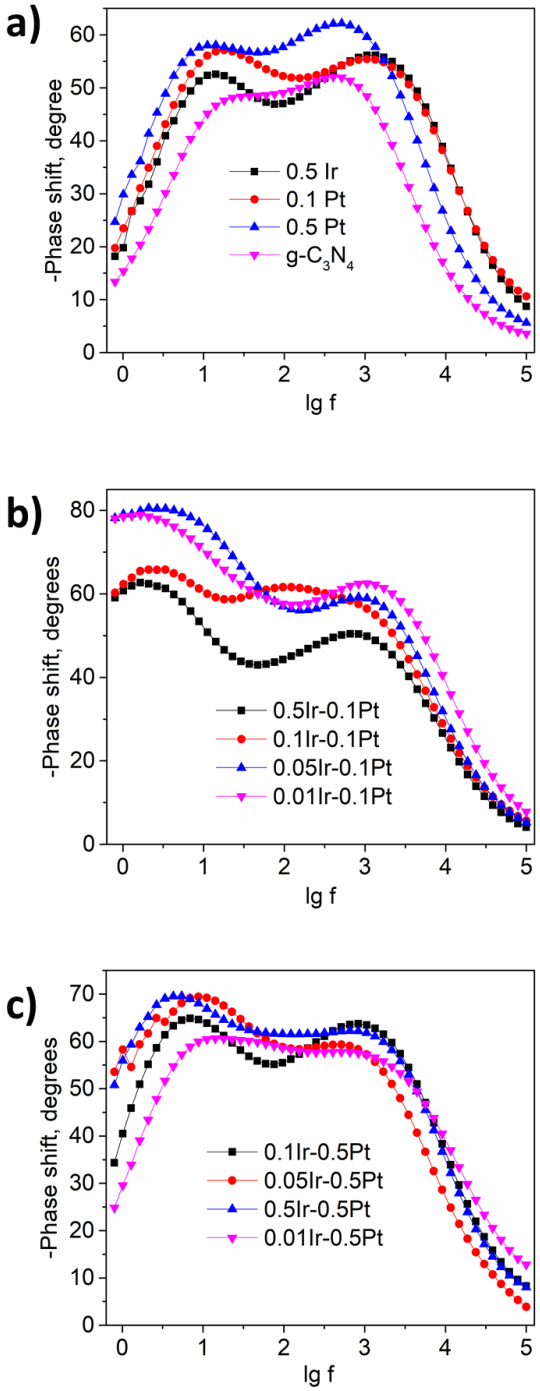

Figure 9 The Bode plot recoded in the photoelectrochemical cells with g-C_3N_4 and monometallic photoelectrodes (a); *y*Ir–0.1Pt (b); *y*Ir–0.5Pt as working electrodes (c). The external potential is 200 mV, the amplitude is 10 mV.

 DOI: 10.15826/chimtech.2024.11.2.08

Table 4 Lifetimes of charge carriers measured in the presence of the tested electrodes in 0.5 M Na_2SO_4.

Working electrode	τ_1 (ms)	τ_2 (ms)
g-C_3N_4	12±2	0.20±0.06
0.1 Pt	13±3	0.11±0.07
0.5 Pt	20±4	0.2±0.1
0.5 Ir	16±4	0.11±0.02
0.01Ir–0.1Pt	13±3	0.11±0.07
0.05Ir–0.1Pt	64±6	0.09±0.03
0.1Ir–0.1Pt	113±4	0.3±0.2
0.5Ir–0.1Pt	117±5	0.19±0.01
0.01Ir–0.5Pt	18±4	0.15±0.01
0.05Ir–0.5Pt	21±4	0.11±0.08
0.1Ir–0.5Pt	30±5	0.2±0.1
0.5Ir–0.5Pt	36±5	0.14±0.04

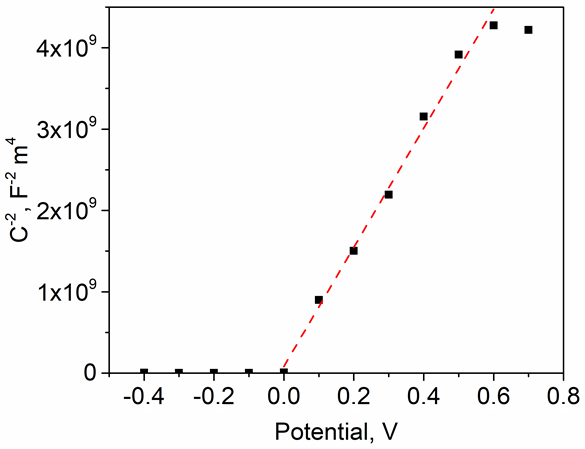

Figure 10 Typical Mott-Schottky plot recorded in the photoelectrochemical cell with 0.5Pt as the working electrode.

Table 5 Flat-band potential and $N{\cdot}\varepsilon$ estimated from the Mott-Schottky plots for all tested photoelectrochemical cells.

Working electrode	J_{sc} (mA/cm²)	V_{fb} (V)	$N{\cdot}\varepsilon$ (m^{-3})
g-C_3N_4	0.571	−0.15±0.03	(1.1±0.1)10^{19}
0.1 Pt	0.353	−0.12±0.02	(2.2±0.1)10^{20}
0.5 Pt	0.280	−0.04±0.01	(1.9±0.1)10^{20}
0.5 Ir	0.339	−0.09±0.05	(4.9±0.7)10^{19}
0.01Ir–0.1Pt	0.028	−0.14±0.03	(1.4±0.2)10^{20}
0.05Ir–0.1Pt	0.016	−0.19±0.03	(1.0±0.1)10^{20}
0.1Ir–0.1Pt	0.077	−0.22±0.05	(3.7±0.6)10^{19}
0.5Ir–0.1Pt	0.077	−0.17±0.08	(1.4±0.2)10^{19}
0.01Ir–0.5Pt	0.106	−0.04±0.01	(6.2±0.7)10^{19}
0.05Ir–0.5Pt	0.129	−0.07±0.03	(1.26± 0.08)10^{20}
0.1Ir–0.5Pt	0.117	−0.06±0.03	(8.0±0.5)10^{19}
0.5Ir–0.5Pt	0.085	−0.08±0.03	(1.2±0.1)10^{20}

Another important parameter calculated from the Mott-Schottky plots is the number of electrons. Unfortunately, we can only estimate the product of the electron number and the dielectric constant. Both values depend on the composition of the photoelectrode. Table 5 shows that $N{\cdot}\varepsilon$ increases with the deposition of noble metal on the surface of g-C_3N_4. At the same time, the energy required for the electron transfer from the noble metal to the external circuit increases; hence, the short-circuit current density decreases. For the *y*Ir–0.1Pt samples, the product of N and ε decreases with increasing Ir content in the sample. For the *y*Ir–0.5Pt set, there are no correlations between the product of N and ε and Ir content or other characteristics.

4. Limitations

This work has several limitations. First of all, we are talking about the accuracy of electrochemical measurements using the impedance method. Unfortunately, it is not possible to obtain more accurate information on the lifetime of charge carriers. The second difficulty is the impossibility of determining the dielectric constant of the photocatalysts, which makes it possible to determine the product of the number of charges and the dielectric constant of the photocatalysts. The third difficulty is the low intensity of the iridium peaks in samples with low iridium content, which makes it impossible to identify its charge state.

5. Conclusions

In this work, the optimisation of the electrolyte composition for testing the g-C_3N_4 based electrodes was carried out. In organic media, such as aqueous and basic solutions of triethanolamine, low current values were obtained. Of the inorganic solutions, 0.5 M Na_2SO_4 yielded the best results and was used for further experiments. Graphitic carbon nitride was then modified with Pt or with Ir and Pt. The photoelectrochemical properties of the resulting photoelectrodes were tested. It was shown that in the case of monometallic co-catalysts, the deposition of noble metal is accompanied by a decrease in the short-circuit current density and an increase in the open-circuit voltage. The simultaneous presence of bimetallic co-catalysts can have a significant effect on the semiconductor's electronic structure and photogalvanic properties. It should be noted that Ir deposition also leads to a decrease in short circuit current density. However, there are some correlations between the shunt current density and the oxidation state of the noble metals. A linear correlation between Pt^0/Pt^0+Pt^{2+} and J_{sc} was observed. It was also shown that the presence of Ir in the form of Ir^{3+} favours the photocurrent generation. The samples obtained were studied by impedance spectroscopy. Overall, the trends in the resistivity variations and the short-circuit current density are opposite to those according to Ohm's law. The equivalent circuit was proposed. For bimetallic co-catalysts, R_1 reflects the resistance of the charge transfer from Pt to the FTO, R_2 can be attributed to the electron transfer from Ir-containing phases to the FTO, R_3 includes the resistance of the charge transfer from the FTO to the external circuit,

 DOI: 10.15826/chimtech.2024.11.2.08

from the counter electrode to the electrolyte, etc. In addition, Mott-Schottky analysis was used to characterise the samples. All samples tested are n-type semiconductors. The deposition of 0.1% Pt does not change the flat band potential.

• Supplementary materials

No supplementary materials are available.

• Funding

This work was funded by the Russian Science Foundation (Grant No. 21-13-00314; https://rscf.ru/en/project/21-13-00314/).

• Acknowledgments

The authors thank Sidorenko N.D. for the preparation of Ir-containing photocatalysts, Dr. Vasilchenko D.B. for the synthesis of Pt-contained samples and g-C_3N_4, Dr. Saraev A.A. for the XPS analysis.

• Author contributions

Conceptualization: E.A.K., D.V.M.
Data curation: D.V.M., V.A.L.
Formal Analysis: V.A.L.
Funding acquisition: E.A.K.
Investigation: V.A.L.
Methodology: D.V.M.
Project administration: D.V.M., E.A.K.
Resources: E.A.K.
Software: E.A.K.
Supervision: E.A.K.
Validation: V.A.L.
Visualization: D.V.M.
Writing – original draft: D.V.M., V.A.L.
Writing – review & editing: D.V.M., E.A.K.

• Conflict of interest

The authors declare no conflict of interest.

• Additional information

Author IDs:
Dina V. Markovskaya, Scopus ID 55895307200;
Victoria A. Lomakina, Scopus ID 57485885500;
Ekaterina A. Kozlova, Scopus ID 12244601300.

Website:
Boreskov Institute of Catalysis, https://catalysis.ru.

References

1. Dada M, Popoola P. Recent advances in solar photovoltaic materials and systems for energy storage applications: a review. Beni-Suef Univ J Basic Appl Sci. 2023;12(66). doi:10.1186/s43088-023-00405-5
2. Wen J, Xie J, Chen X, Li X. A review on g-C_3N_4-based photocatalysts. Appl Surf Sci. 2017;391:72–123. doi:10.1016/j.apsusc.2016.07.030.
3. Qin DD, Quan JJ, Duan SF, San Martin J, Lin Y, Zhu X, Yao XQ, Su JZ, Rodríguez-Gutiérrez I, Tao CL, Yan Y. High-performance photoelectrochemical water oxidation with phosphorus-doped and metal phosphide cocatalyst-modified g-C_3N_4 formation through gas treatment. ChemSusChem. 2019;21;12(4):898–907. doi:10.1002/cssc.201802382
4. Amedlous A, Majdoub M, Amaterz E, Anfar Z, Benlhachemi A. Synergistic effect of g-C_3N_4 nanosheets/Ag_3PO_4 microcubes as efficient n-p-type heterostructure based photoanode for photoelectrocatalytic dye degradation. J Photochem Photobio A Chem. 2021;409:113127. doi:10.1016/j.jphotochem.2020.113127
5. Zhuang H, Lin J, Xu M, Xu W, Liu X. Construction of g-C_3N_4-based photoelectrodes towards photoelectrochemical water splitting: A review. J. Alloys Compd. 2023;969:172302. doi:10.1016/j.jallcom.2023.172302
6. Xiao J, Zhang X, Li Y. A ternary g-C_3N_4/Pt/ZnO photoanode for efficient photoelectrochemical water splitting. Int J Hydrog Energy. 2015;40(30):9080–9087. doi10.1016/j.ijhydene.2015.05.122.
7. Li W, Chu X-S, Wang F, Dang Y-Y, Liu X-Y, Wang H-C, Wang C. Enhanced cocatalyst-support interaction and promoted electron transfer of 3D porous g-C_3N_4/GO-M (Au, Pd, Pt) composite catalysts for hydrogen evolution. Appl Catal B Environm. 2021;288:120034. doi:10.1016/j.apcatb.2021.120034
8. Li H, Xia Z, Chen J, Lei L, Xing J. Constructing ternary CdS/reduced graphene oxide/TiO_2 nanotube arrays hybrids for enhanced visible-light-driven photoelectrochemical and photocatalytic activity. Appl Catal B: Environm. 2015;168–169:105–113. doi:10.1016/j.apcatb.2014.12.029
9. Liang S, Xia Y, Zhu S, Zheng S, He Y, Bi J, Liu M, Wu L. Au and Pt co-loaded g-C_3N_4 nanosheets for enhanced photocatalytic hydrogen production under visible light irradiation. Appl Surf Sci. 2015;358:304–312. doi:10.1016/j.apsusc.2015.08.035
10. Bu Y, Chen Z, Li W. Using electrochemical methods to study the promotion mechanism of the photoelectric conversion performance of Ag-modified mesoporous g-C_3N_4 heterojunction material. Appl Catal BEnvironm. 2014;144:622–630. doi:10.1016/j.apcatb.2013.07.066
11. Markovskaya DV, Zhurenok AV, Kozlova EA. Rate of photocatalytic hydrogen evolution and photovoltaic characteristics as a function of the nature and concentration of the electrolyte. Russ J Phys Chem A. 2022:96(5):1093–1098.doi:10.1134/S003602442205020X
12. Wang W, Kou X, Li T, Zhao R, Su Y. Tunable heptazine/triazine feature of nitrogen deficient graphitic carbon nitride for electronic modulation and boosting photocatalytic hydrogen evolution. J Photochem Photobiol A Chem. 2023;435:114308. doi:10.1016/j.jphotochem.2022.114308
13. Yang H, Sun S, Duan R, Yang B, Yang M, Qi X, Cai C, Yun D, Yang Q, Cui J. Mechanism insight into enhanced photocatalytic hydrogen production by nitrogen vacancy-induced creating built-in electric field in porous graphitic carbon nitride nanosheets. Appl Surf Sci. 2023;631:157544. doi:10.1016/j.apsusc.2023.157544
14. Ruan X, Wang Z, Wei Z, Zhang H, Zhang L, Zhao X, Singh DJ, Zhao J, Cui X, Zheng W. Electron cloud density localized graphitic carbon nitride with enhanced optical absorption and carrier separation towards photocatalytic hydrogen evolution. Appl Surf Sci. 2022;601:154294. doi:10.1016/j.apsusc.2022.154294
15. Sherryna A, Tahir M, Yamani Z, Alias H. 2D/2D NiAl LDH integrated graphitic carbon nitride with robust interfacial

contact for driving photocatalytic hydrogen production. Mater Today: Proceedings. 2023. doi:10.1016/j.matpr.2023.08.133
16. Shi J, Wang H, Nie J, Yang T, Ju C, Pu K, Shi J, Zhao T, Li H, Xue J. Alkali-assisted engineering of ultrathin graphite phase carbon nitride nanosheets with carbon vacancy and cyano group for significantly promoting photocatalytic hydrogen peroxide generation under visible light: Fast electron transfer channel. J Colloid Interf Sci. 2023;643:47–61. doi:10.1016/j.jcis.2023.03.209
17. Chen Y, Lei L, Gong Y, Wang H, Fan H, Wang W. Enhanced electron delocalization on pyrimidine doped graphitic carbon nitride for boosting photocatalytic hydrogen evolution. Int J Hydrog Energy. 2024;51A:1058–1068. doi:10.1016/j.ijhydene.2023.07.147
18. Xu M, Meng D, Yousaf AB, Ruan X, Cui X. Superior hydrophilic porous graphitic carbon nitride for enhanced photocatalytic hydrogen evolution. Mater Lett. 2023;350:134888. doi:10.1016/j.matlet.2023.134888
19. Baranowska D, Mijowska E, Zielinska B. Promotion of photocatalytic hydrogen evolution induced by graphitic carbon nitride transformation from 2D flakes to 1D nanowires. Mater Res Bull. 2023;163:112210. doi:10.1016/j.materresbull.2023.112210
20. Yang Y, Li S, Mao Y, Dang Y, Jiao Z, Xu K. Post-functionalization of graphitic carbon nitride for highly efficient photocatalytic hydrogen evolution. J Fuel Chem Technol. 2023;51(2):205–214. doi:10.1016/S1872-5813(22)60036-7
21. Li J, Peng H, Luo B, Cao J, Ma L, Jing D. The enhanced photocatalytic and photothermal effects of Ti_3C_2 Mxene quantum dot/macroscopic porous graphitic carbon nitride heterojunction for Hydrogen Production. J Colloid Interface Sci. 2023;641:309–318. doi:10.1016/j.jcis.2023.03.015.
22. Gao J, Li M, Chen H, Guo L, Li Z, Wang X. Microstructure regulation of graphitic carbon nitride nanotubes via quick thermal polymerization process for photocatalytic hydrogen evolution. J Photochem Photobiol A Chem. 2023;441:114747. doi:10.1016/j.jphotochem.2023.114747
23. Wang T, Wan T, He S, Wang J, Yu M, Jia Y, Tang Q. Facile fabrication of graphitic carbon nitride by solvothermal method with hierarchical structure and high visible light photocatalytic activity. J Taiwan Inst Chem E. 2023;145:104773. doi:10.1016/j.jtice.2023.104773
24. Wei J, Zhao R, Luo D, Lu X, Dong W, Huang Y, Cheng X, Ni Y. Atomically precise $Ni_6(SC_2H_4Ph)_{12}$ nanoclusters on graphitic carbon nitride nanosheets for boosting photocatalytic hydrogen evolution. J Colloid Interf Sci. 2023;631(A):212–221. doi:10.1016/j.jcis.2022.11.010
25. Baranowska D, Zielinkiewicz K, Kedzierski T, Mijowska E, Zielinska B. Heterostructure based on exfoliated graphitic carbon nitride coated by porous carbon for photocatalytic H_2 evolution. Int J Hydrog Energy. 2022;47(84):35666–35679. doi:10.1016/j.ijhydene.2022.08.15
26. Yu Z, Guan C, Yue X, Xiang Q. Infiltration of C-ring into crystalline carbon nitride S-scheme homojunction for photocatalytic hydrogen evolution. Chinese J Catal. 2023;50:361–371. doi:10.1016/S1872-2067(23)64448-1.
27. Lei L, Fan H, Jia Y, Wu X, Zhong Q, Wang W. Ultrafast charge-transfer at interfaces between 2D graphitic carbon nitride thin film and carbon fiber towards enhanced photocatalytic hydrogen evolution. Appl Surf Sci. 2022;606:154938. doi:10.1016/j.apsusc.2022.154938
28. Das B, Devi M, Deb S, Dhar SS. Boosting photocatalytic property of graphitic carbon nitride with metal complex fabrication for efficient degradation of organic pollutants. Chemosphere. 2023;323:138230. doi:10.1016/j.chemosphere.2023.138230
29. Cheng C, Shi J, Mao L, Dong C-L, Huang Y-C, Zong S, Liu J, Shen S, Guo L. Ultrathin porous graphitic carbon nitride from recrystallized precursor toward significantly enhanced photocatalytic water splitting. J Colloid Interf Sci. 2023;637:271–282. doi:10.1016/j.jcis.2023.01.098
30. Luo M, Jiang G, Yu M, Yan Y, Qin Z, Li Y, Zhang Q. Constructing crystalline homophase carbon nitride S-scheme heterojunctions for efficient photocatalytic hydrogen evolution. J Mater Sci Technol. 2023;161:220–232. doi:10.1016/j.jmst.2023.03.038
31. Chang X, Fan H, Zhu S, Lei L, Wu X, Feng C, Wang W, Ma L. Engineering doping and defect in graphitic carbon nitride by one-pot method for enhanced photocatalytic hydrogen evolution. Ceram Inter. 2023;49(4):6729–6738. doi:10.1016/j.ceramint.2022.10.151
32. Xu X, Feng X, Wang W, Song K, Ma D, Zhou Y, Shi Y-W. Construction of II-type and Z-scheme binding structure in P-doped graphitic carbon nitride loaded with ZnO and ZnTCPP boosting photocatalytic hydrogen evolution. J Colloid Interf Sci. 2023;651:669–677. doi:10.1016/j.jcis.2023.08.033
33. Wang T, Wan T, He S, Wang J, Yu M, Jia Y, Tang Q. Fabrication of structural defects and carboxyl groups on graphitic carbon nitride with enhanced visible light photocatalytic activity. J Environ Chem Eng. 2023;11(3):2213–3437. doi:10.1016/j.jece.2023.110050
34. Inoue T, Chuaicham C, Saito N, Ohtani B, Sasaki K. Z-scheme heterojunction of graphitic carbon nitride and calcium ferrite in converter slag for the photocatalytic imidacloprid degradation and hydrogen evolution. J Photochem Photobiol A Chem. 2023;440:114644. doi:10.1016/j.jphotochem.2023.114644
35. Markovskaya DV, Kozlova EA. Application of the Similarity Theory to Analysis of Photocatalytic Hydrogen Production and Photocurrent Generation. Chimica Techno Acta. 2023;10(2):202310203:1–21. doi:10.15826/chimtech.2023.10.2.03
36. Sidorenko ND, Topchiyan PA, Saraev AA, Gerasimov EY, Zhurenok AV, Vasilchenko DB, Kozlova EA. Bimetallic Pt-IrOx/g-C_3N_4 photocatalysts for the highly efficient overall water splitting under visible light. Catalysts. 2024;14(4):225. doi:10.3390/catal14040225
37. Markovskaya DV, Zhurenok AV, Cherepanova SV, Kozlova EA. Solid Solutions of CdS and ZnS: Comparing Photocatalytic Activity and Photocurrent Generation. Appl Surf Sci Adv 2021;4:100076:1–8. doi:10.1016/j.apsadv.2021.100076
38. Kamat PV, Tvrdy K, Baker DR, Padich JG. Beyong photovoltaics: semiconductor nanoarchitectures for liquid-junction solar cells. Chem Rev. 2010;110:6664–6688. doi:10.1016/j.mssp.2021.105717.
39. Baudys M, Paušová S, Praus P, Brezová V, Dvoranová D, Barbieriková Z, Krýsa J. Graphitic Carbon Nitride for Photocatalytic Air Treatment. Mater. 2020;13(13):3038. doi:10.3390/ma13133038
40. Ofuonye B, Lee J, Yan M, Sun C, Zuo J-M, Adesida I. Electrical and microstructural properties of thermally annealed Ni/Au and Ni/Pt/Au Schottky contacts on AlGaN/GaN heterostructures. Semiconductor Sci Technol. 2014;29(9):095005. doi:10.1088/0268-1242/29/9/095005
41. Fei X, Zhang L, Yu J, Zhu B. DFT Study on Regulating the Electronic Structure and CO_2 Reduction Reaction in Bi-OBr/Sulphur-Doped G-C_3N_4 S-Scheme Heterojunctions. Nanotechnology for Energy Applications. 2021; 3:698351. doi:10.3389/fnano.2021.698351
42. Kann S, Takemoto S, Kaneko K, Takahashi I, Sugimoto M, Shinohe T, Fujita S. Electrical properties of α-Ir_2O_3/α-Ga_2O_3 pn heterojunction diode and band alignment of the heterostructure. Appl Phys Lett. 2018;113:212104. doi:10.1063/1.5054054
43. Markovskaya D, Sidorenko N, Zhurenok A, Kozlova E. Studying Effects of External Conditions of Electrochemical Measurements on the Photoelectrochemical Properties of Semiconductors: Cyclic Voltammetry, Impedance Spectroscopy, and Mott-Schottky Method. Electrochem Mater Technol. 2023;2(2):20232013:1–14. doi:10.15826/elmattech.2023.2.013
44. Kaneko K, Fujita S. Novel p-type oxides with corundum structure for gallium oxide electronics. J Mater Res. 2022;37:651–659. doi:10.1557/s43578-021-00439-4